

H₂ molecular gas in the old planetary nebula NGC 3587

G. Ramos-Larios^{★1}, M. A. Guerrero², J. A. Toalá³, S. Akas⁴ and X. Fang⁵

¹*Instituto de Astronomía y Meteorología, CUCEI, Universidad de Guadalajara, Av. Vallarta 2602, Col. Arcos Vallarta, 44130 Guadalajara, Mexico*

²*Instituto de Astrofísica de Andalucía, IAA-CSIC, C/Glorieta de la Astronomía s/n, 18008 Granada, Spain*

³*Instituto de Radioastronomía y Astrofísica, UNAM, Ant. Carretera a Pátzcuaro 8701, Ex-Hda. San José de la Huerta, Morelia 58089, Mich., Mexico*

⁴*Institute for Astronomy, Astrophysics, Space Applications and Remote Sensing, National Observatory of Athens, GR 15236 Penteli, Greece*

⁵*National Astronomical Observatories, Chinese Academy of Sciences, 20A Datun Road, Chaoyang District, Beijing, China*

19 December 2023

ABSTRACT

The acquisition of high-quality deep images of planetary nebulae (PNe) has allowed the detection of a wealth of small-scale features, which highlight the complexity of the formation history and physical processes shaping PNe. Here we present the discovery of three groups of clumps embedded within the nebular shell of the evolved PN NGC 3587, the Owl Nebula, that had escaped previous detections. The analysis of multi-wavelength GEMINI GMOS, NOT ALFOSC, Aristarchos Andor optical, CFHT WIRCam and *Spitzer* IRAC and MIPS infrared (IR) images indicates that these clumps are formed by material denser and colder than the surrounding nebula, with a notable content of molecular H₂, but negligible or null amounts of dust. The presence of H₂-rich pockets embedded within the ionized shell of this evolved PN is suggestive of the survival of high-density condensations of material created at the onset of the PN stage.

Key words: (ISM:) planetary nebulae: general — planetary nebulae: individual: NGC 3587 — ISM: molecules — ISM: jets and outflows — ISM: lines and bands — infrared: ISM

1 INTRODUCTION

Molecules are commonly found in the interstellar medium (ISM), frequently associated with star forming regions, dense and vast molecular clouds, and the circumstellar environment around evolved stars, to name a few. Among the large number of molecules in the ISM, one of the most abundant is molecular hydrogen (H₂). Its formation occurs through reactions on the surface of dust grains, which act as catalyst to absorb the energy excess that is released when a new H₂ molecule is formed, surviving to photo-dissociation in not too dense environments. Multiple transitions of this molecule can be detected at infrared (IR) wavelengths. The near-IR H₂ 1–0 S(1) λ 2.122 μ m emission line is the brightest and most easily detected, although the H₂ 2–1 S(1), H₂ 1–0 S(2), H₂ 1–0 S(0), H₂ 1–0 S(3), and H₂ 2–1 S(3) near-IR transitions can be also detected. In the mid-IR, H₂ 0–0 transitions from the S(2) to the S(7) lines emission have also been observed, with the H₂ 0–0 S(3) λ 9.66 μ m line being among the brightest.

These emission lines are routinely detected in planetary nebulae (PNe). Since the pioneer work of Isaacman (1984), many succeeding near-IR imaging and spectroscopic H₂ surveys of PNe have been published (Webster et al. 1988; Latter et al. 1995; Kastner et al. 1996; Hora, Latter, & Deutsch 1999; Guerrero et al. 2000; Ramos-Larios et al. 2017; Gledhill et al. 2018, and references therein), as well as mid-IR ones (e.g., Mata et al. 2016; Otsuka et al. 2017; De Marco et al. 2022). The detector technological advances and increasing telescope apertures have played an important role

in the detection of new H₂-emitting PNe. Indeed, many PNe that were previously undetected in H₂ surveys (e.g., A 66, NGC 6543, NGC 7009, NGC 7662 or M 2–48, Webster et al. 1988; Kastner et al. 1996, and references therein) are now known to present H₂ emission associated with low-ionization structures (e.g., K 4–47, NGC 6543, NGC 7009, and NGC 7662, Akas, Gonçalves, & Ramos-Larios 2017; Fang et al. 2018; Akas et al. 2020a), the so-called LIS (Gonçalves, Corradi, & Mampaso 2001), or with dense knots and clumps that are embedded within ionized material in ring-like structures (e.g., NGC 650–51, Marquez-Lugo et al. 2013).

Among the PNe that exhibit H₂ emission there seem to be two types: those that exhibit thousands of clumps (group A; e.g., NGC 2346 and NGC 3132; Manchado et al. 2015; De Marco et al. 2022) while others are detected to harbour a few H₂-emitting knots (group B; e.g., NGC 7662, NGC 6543, K 4–47, NGC 6778, NGC 3242, NGC 6826, NGC 6818, NGC 7354 and Hu 1–2; Fang et al. 2018). Group A is characterized by old PNe with ages >7000 yr and H₂ clumps with sizes of $[1–4] \times 10^{15}$ cm (Akas et al. 2020b), whereas PNe in group B are younger (<2000 yr) and have clump sizes larger than 10^{16} cm.

Here we report the discovery of a number of clumps embedded within ionized material detected in optical low-excitation ionic and near-IR H₂ molecular line emission in NGC 3587, a.k.a. the Owl Nebula, which were undetected in early studies (Kastner et al. 1996). NGC 3587 is a triple-shell PN consisting of an elliptical inner shell with the characteristic "owl eyes and beak", a round envelope, and an outer halo (Guerrero et al. 2003). The latter is asymmetrical, with a bow-shock like shape along the direction of motion of the central star revealing the interaction of the nebula with the ISM. Several works outline precisely its physical structure observed through many

★ E-mail: gerardo@astro.iam.udg.mx

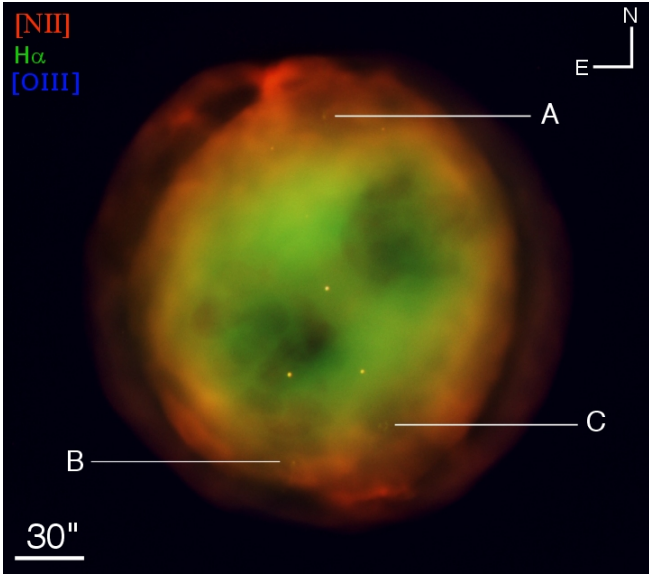


Figure 1. NOT ALFOSC colour-composite picture of NGC 3587 of [N II] (red), H α (green) and [O III] (blue) images (see details in Sec. 2.1.1). The picture reveals three barely visible small discrete regions, labelled as A, B and C, that contrast with the large-scale filaments and bright and dark patches of the main nebula.

emission lines (Sabbadin et al. 1985), including a complete analysis of the density distribution (Cuesta & Phillips 2000) and a morpho-kinematic modeling that describes accurately the dynamics of this highly evolved PN and highlight the presence of a series of internal cavities (García-Díaz et al. 2018). Interestingly, NGC 3587 is an evolved PNe, with an estimated kinematic age $\approx 10,400$ yr and a linear size for its main nebula ≈ 0.86 pc (Guerrero et al. 2003) at the *Gaia* distance of 810 ± 30 pc. That is, it should be part of group A of the H $_2$ -emitting PNe, but as we will demonstrate its number of H $_2$ -emitting clumps is not large.

In order to investigate the nature of the newly discovered molecular hydrogen clumps and its spatial correlation with the ionized nebula and possible dust content, we have collected a large amount of high-quality observational material in the optical and IR range. A general and brief description of the available observations is presented in Section 2, with the results described in Section 3. The discussion is presented in Section 4 and the final conclusions in Section 5.

2 OBSERVATIONS

2.1 Optical Imaging

In the following we present the details of the optical images. A summary of the optical observations is presented in Table 1.

2.1.1 Nordic Optical Telescope

The ALhambra Faint Object Spectrograph and Camera (ALFOSC) at the 2.56-m Nordic Optical Telescope (NOT) in the Observatorio de Roque de los Muchachos (ORM, La Palma, Spain) was used to obtain a series of images of NGC 3587 in the [N II], H α and [O III] emission lines on 2018 June 20. The detector used was a 2K \times 2K e2v CCD with plate scale 0.21 arcsec pix^{-1} and a field of view (FoV) of $6'.5 \times 6'.5$. The central wavelengths and bandwidths of the narrow-band filters are $\lambda_c = 6583$ Å and $\Delta\lambda = 13$ Å for [N II], $\lambda_c = 6565$ Å and $\Delta\lambda = 13$ Å for

Table 1. Details of the optical and IR imaging.

Telescope	Instrument	Filter	λ_c (Å)	$\Delta\lambda$ (Å)
NOT	ALFOSC	[O III]	5007	30
		H α	6567	13
		[N II]	6588	13
GEMINI	GMOS	<i>g</i> (G0301)	4744	1700
		H α (G0310)	6576	140
		<i>r</i> (G0303)	6298	1700
		[O I]	6304	30
Aristarchos	Andor ikon-L	[S II]	6727	40
		K_c	22180	330
CFHT	WIRCcam	H $_2$	21220	320
		Br $_\gamma$	21660	300
		3.6	35500	7500
<i>Spitzer</i>	IRAC	4.5	44930	19015
		8.0	78720	29050
		24	240000	50000

H α , and $\lambda_c = 5007$ Å and $\Delta\lambda = 30$ Å for [O III]. The spatial resolution achieved during the observations, as determined from the FWHM of stars in the FoV, was ≈ 0.85 arcsec. Three individual frames with integration times of 600 s were taken for the [N II] and H α filters, leading to total exposure times of 1800 s, whilst three frames with integration times of 200 s were used for the [O III] for a total exposure time of 600 s.

The NOT images were bias-subtracted and flat-fielded using twilight flats employing standard IRAF¹ routines (Tody 1993). A NOT ALFOSC colour-composite picture of the Owl Nebula in the light of H α , [N II] and [O III] is presented in Figure 1.

2.1.2 Gemini North Telescope

Very high-angular-resolution optical images of NGC 3587 were acquired at the Gemini North Observatory with the Gemini North Multi-Object Spectrographs (GMOS-N) on April 15, 2009 in the narrow-band H α + [N II] G0310 filter and broad-band *r*-SDSS (G0303) and *g*-SDSS (G0301) filters. The exposure times were 8 \times 90 s, 16 \times 30 s and 16 \times 30 s, respectively, on 2 \times 2 binning. The unbinned detector array consisted of three 2048 \times 4608 EEV chips for a total of 6144 \times 4608 pixels arranged in a row with ~ 0.5 mm gaps with pixel size of 13.5×13.5 μm , plate scale of $0''.0727$ pixel^{-1} , and FoV of $5'.5 \times 5'.5$. The seeing during the observations, as determined from the FWHM of stars in the FoV, was ≈ 0.65 arcsec. The Gemini images were processed employing *gmosaic* and *gemtools* tasks and standard IRAF routines. A Gemini North GMOS colour-composite picture of the Owl Nebula is presented in Figure 2.

2.1.3 Aristarchos Telescope

The 2.3m Aristarchos telescope at the Helmos Observatory (Greece) was used to obtain a series of images in the [O I] $\lambda 6300$ and [S II] $\lambda 6716, 6731$ emission lines on 2023 July 17. The camera used was an Andor ikon-L with a CCD e2v CCD42-40 detector, which included 2048 \times 2048 pixels² with 13.5 μm pixel size, resulting to a

¹ The Image Reduction and Analysis Facility, IRAF, is distributed by the National Optical Astronomy Observatory, which is operated by the Association of Universities for Research in Astronomy (AURA) under cooperative agreement with the National Science Foundation.

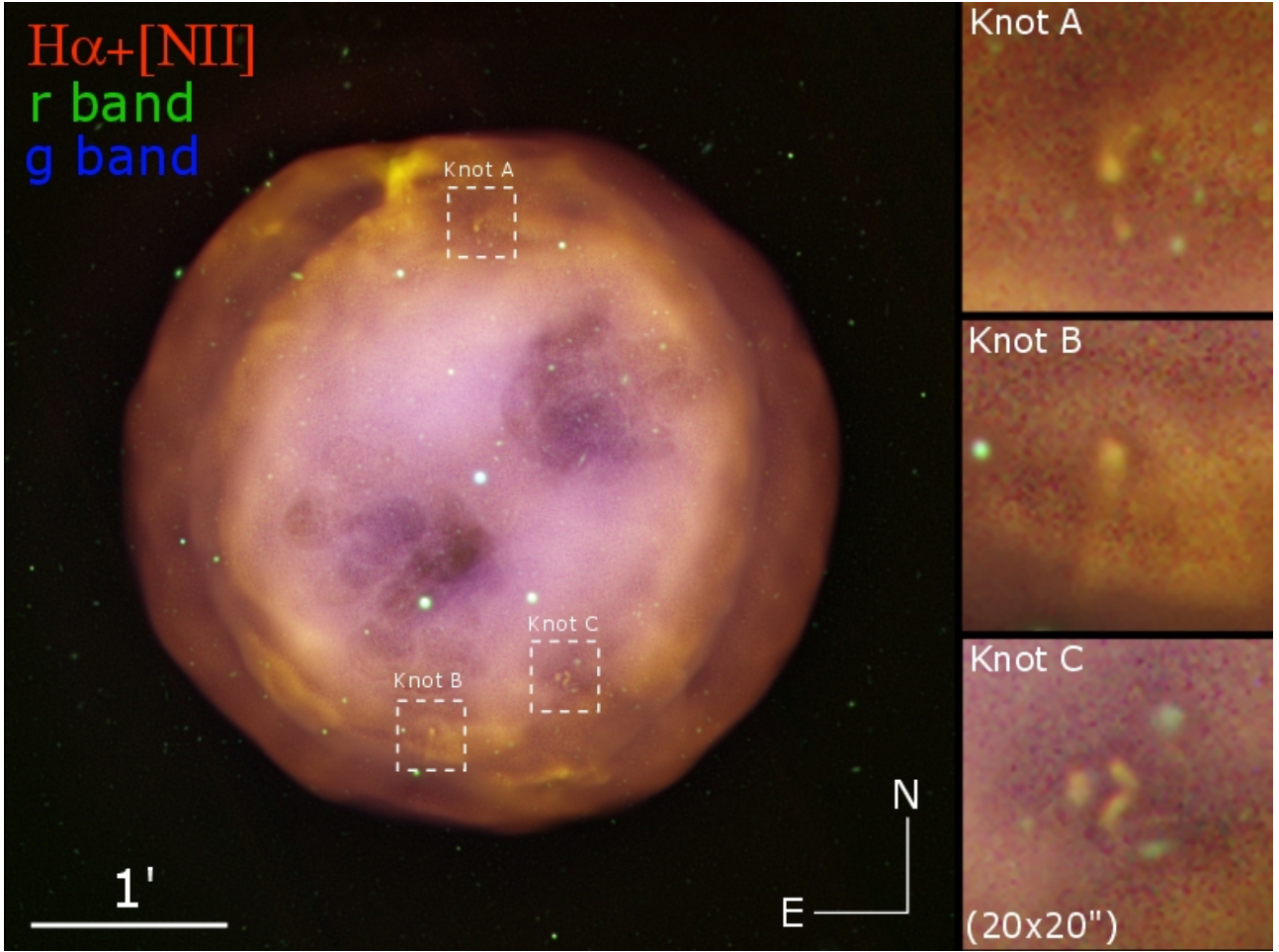


Figure 2. (left) Gemini North GMOS high-resolution colour-composite picture of NGC 3587 in the light of the $H\alpha$ + $[N\ II]$ (red), r -SDSS (green), and g -SDSS (blue) filters, and (right) insets of the $20''\times 20''$ squared boxes overlaid on the picture around the position of the areas of lumpy material denoted as A, B and C in Figure 1. Their “unusual” shapes are emphasized in these zoomed views, with a bow-shock-like structure apparently associated with feature B. The image has been processed using unsharp masking techniques to emphasize small details in the main nebula.

spatial scale of $0''.16\ \text{pix}^{-1}$ and a FoV of $5'.5\times 5'.5$. In this case, the resolution achieved during the observations, as determined from the FWHM of stars in the FoV, was ≈ 1.75 arcsec. The central wavelengths and bandwidths of the filters are $\lambda_c=6304\ \text{\AA}$ and $\Delta\lambda=30\ \text{\AA}$ for $[O\ I]$ and $\lambda_c=6727\ \text{\AA}$ and $\Delta\lambda=40\ \text{\AA}$ for $[S\ II]$. The $[O\ I]$ $6300\ \text{\AA}$ and $[S\ II]$ $6716+6731\ \text{\AA}$ images were obtained with exposure times of 2×900 sec and 900 sec, respectively.

Standard IRAF routines were followed for the images processing, which includes bias subtraction, flat fielding correction, bad-pixel screening, and cosmic-ray removal. Figure 3 displays a 65×65 arcsec² section of the $[O\ I]$ image towards the northern region of the Owl Nebula.

2.2 IR Imaging

2.2.1 CFHT WIRCam

The Wide-field InfraRed Camera (WIRCam) (Puget et al. 2004) is an state-of-art near-IR wide-field imaging instrument mounted at the prime focus of the 3.6m Canada-France-Hawaii Telescope (CFHT). WIRCam consists of a mosaic of four HAWAII2-RG detectors, each containing 2048×2048 pixels, with a sampling of $0.3\ \text{arcsec}\ \text{pix}^{-1}$ and an impressive FoV of $20'.0\times 20'.0$. A series of exposures in

the narrow-band filters of K_c ($\lambda_c=2.218\ \mu\text{m}$ and $\Delta\lambda=0.033\ \mu\text{m}$), H_2 ($\lambda_c=2.122\ \mu\text{m}$ and $\Delta\lambda=0.032\ \mu\text{m}$), and $\text{Br}\gamma$ ($\lambda_c=2.166\ \mu\text{m}$ and $\Delta\lambda=0.030\ \mu\text{m}$) were acquired on 2013 December 22 and 25 (program ID 13BS01, P.I. Yong Zhang). Sixteen images with individual exposure times of $65\ \text{s}$ for H_2 , whilst twelve and eight frames with exposures of $60\ \text{s}$ for the $\text{Br}\gamma$ and K_c filters respectively were combined in order to improve the signal-to-noise (S/N) ratio.

Similarly to the optical imaging obtained at the NOT, all the WIRCam images were reduced following standard IR procedure using IRAF routines, including dark subtraction, flat-field correction, basic cross-talk removal, and sky subtraction for the final combination of each set of images. A colour-composite image of NGC 3587 using the WIRCam narrow-band images is presented in Figure 4-top.

2.2.2 Spitzer IRAC & MIPS

Images from the Infrared Array Camera (IRAC; Fazio et al. 2004) on board *Spitzer* were obtained from the National Aeronautics and Space Administration/Infrared Processing and Analysis Center (NASA/IPAC) Infrared Science Archive (IRSA). IRAC is a four-channel camera capable for simultaneous imaging in broadband filters with central wavelengths $3.6, 4.5, 5.8$ and $8.0\ \mu\text{m}$. The detec-

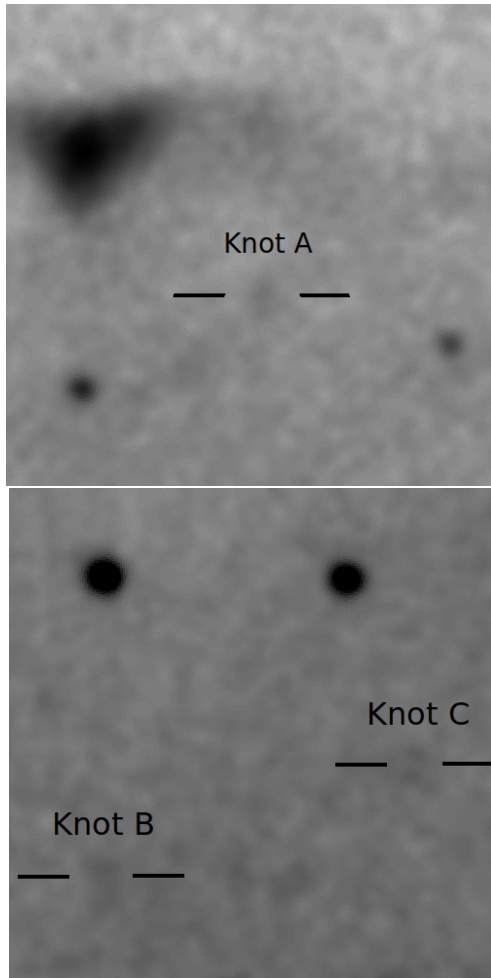


Figure 3. Aristarchos narrow-band [O I] $\lambda 6300$ grayscale images of NGC 3587 centred at clumps A (top), and B and C (bottom). The horizontal lines indicate the position of the clumps. The size of the images is 65×65 arcsec². North is up, east to the left.

tor arrays of 256×256 pixels in size use InSb for the two shorter-wavelength 3.6 and 4.5 μm channels, and Si:As IBC detectors for the two longer-wavelength 5.8 and 8.0 μm channels.

The set of images were acquired on 2004 April 20 as part of Program ID 68 (Studying Stellar Ejecta on the Large Scale using SIRTf-IRAC, PI: Giovanni Fazio). The observations presented here make use only of the filters at 3.6 μm , 4.5 μm and 8 μm (see middle panel in Fig. 4). The more noisy 5.8 μm image was discarded for the final composition.

In addition, we also retrieved a 24 μm image of NGC 3587 obtained with the Multiband Imaging Photometer (MIPS; Rieke et al. 2004) on board *Spitzer*. These data were obtained on 2008 January 8 as part of Program ID 40953 (MIPS Survey of Dust Disks around Hot White Dwarfs, PI: You-Hua Chu). As the IRAC long-wavelength bands, the MIPS 24 μm camera uses the Si:As IBC detector array of 128×128 pixels. The MIPS 24 μm band is mainly dominated by dust continuum, but also the [Ne v] at 24.3 μm and the [O iv] at 25.9 μm lines are strong candidates to MIPS fluxes in nebular components (see Chu et al. 2009).

Colour-composite pictures of NGC 3587 using the *Spitzer* IRAC 3.6 , 4.5 , and 8 μm images, and the *Spitzer* IRAC 4.5 μm and MIPS

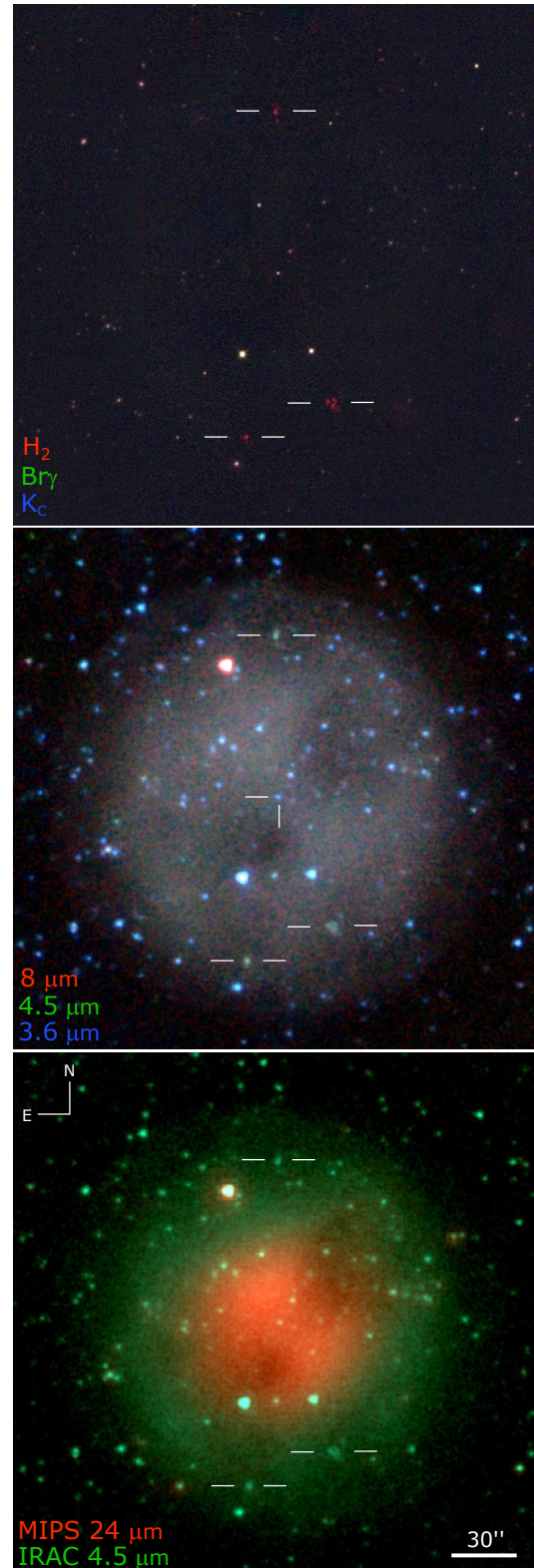


Figure 4. Near- and mid-IR colour-composite pictures of NGC 3587 obtained combining CFHT H_2 (red), $\text{Br}\gamma$ (green), and K_c (blue) images (top), *Spitzer* IRAC 3.6 μm (blue), 4.5 μm (green), and 8 μm (red) images (middle), and *Spitzer* MIPS 24 μm (red) and IRAC 4.5 μm (green) images (bottom). All pictures share the same scale and FoV. The position of the progenitor star is marked at the centre of the middle panel, whilst horizontal lines in the three panels show the position of H_2 molecular hydrogen as clearly denoted in the top panel. Note the conspicuous lack of nebular $\text{Br}\gamma$ emission in the CFHT colour-composite picture (top panel).

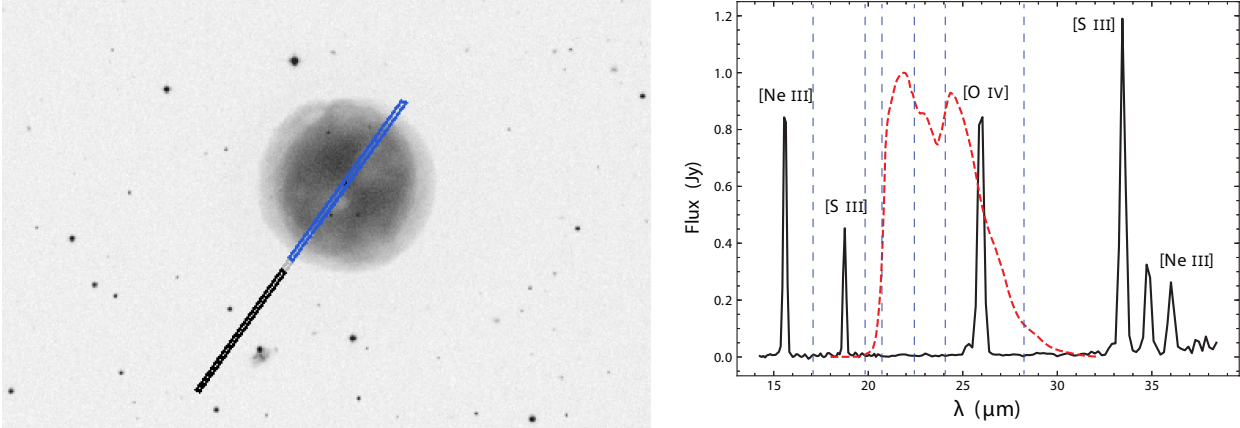


Figure 5. (left) Slit position for the *Spitzer* IRS LL modules (blue) and slit position for background subtraction (black). (right) *Spitzer* background subtracted spectra. The spectral region around 21 μm shows the overlap of the LL1+LL2 spectra. Main ionic lines are identified as well as some H_2 lines in the *S* and *O* transitions marked in dashed blue, like the H_2 0–0 *S*(0) at 28.2188 μm and the H_2 6–5 *O*(16) at 19.8082 μm among others. The MIPS 24 μm transmission curve is also marked with a red dashed line. As mentioned in the text, unfortunately none of the available slits positions intersect the H_2 zones observed in the main nebula.

24 μm images are presented in the middle and bottom panels of Figure 4, respectively.

2.3 IR Spectra

2.3.1 *Spitzer* IRS

Spectroscopic observations obtained with the *Spitzer* Infrared Spectrograph (IRS; Houck et al. 2004) were downloaded from the NASA/IPAC Infrared Science Archive. The instrument consists mainly of four separate modules, the Short-Low (SL) and Short-High (SH) ones, which provide low resolution ($R \sim 60$ –128) spectroscopic capabilities in the spectral range from 5.2 to 38 μm , and the Long-Low (LL) and Long-High (LH) modules, with moderate or high resolution ($R \approx 600$) in the spectral range from 9.9 to 37.2 μm . The set of spectra used here were acquired on 2004 April 17 as part of Program ID: CAL IRS 1406/1406 (Program reserved for IRS calibration observations, PI: Calibration, IRS).

In this work we only present the IRS spectra obtained with the Long-Low LL1 and LL2 modules with suitable slits positions for background subtraction. The plate scale was 5.1 arcsec pix^{-1} and the aperture sizes for the LL1 and LL2 modules were 10.7 \times 168 arcsec² and 10.5 \times 168 arcsec², respectively. The slits had a position angle (PA) of $\approx 145^\circ$. The spectra cover the spectral ranges 14–21.3 μm for LL2 and 19.5–38 μm for LL1 with a resolution $R \sim 57$ –126. All the IRS spectra were processed with the software package Cube Builder for IRS Spectral Mapping (CUBISM; Smith et al. 2007), which is a tool for constructing spectral cubes, maps and arbitrary aperture 1D spectral extractions from sets of mapping mode spectra. The slit position and LL spectra are shown in Figure 5. None of the available slits cover the small H_2 reservoirs in the main nebula.

As for the available SL observations, not presented here, a carefully examination of the spectra obtained with the SL1 and SL2 modules did not found any H_2 emission lines. Since these data lack of suitable positions for background subtraction, they were discarded for subsequent analysis.

3 RESULTS

The narrow- and broad-band optical and IR images of the Owl Nebula presented in the previous section contain information on the nebular emission on a wide excitation range. The overall ionization and physical structure of the Owl Nebula have been the subject of many detailed studies (see Sect. 1). Here we will rather focus on three rather inconspicuous clumps first uncovered in the NOT ALFOSC $\text{H}\alpha$ and [N II] images (see Fig. 1), subsequently confirmed in the Gemini GMOS $\text{H}\alpha$ + [N II] image (Fig. 2) and Aristarchos Andor [O I] images (Fig. 3).

These clumps are labeled as A, B, and C in the NOT ALFOSC $\text{H}\alpha$ and [N II] and Gemini GMOS images presented in Figures 1 and 2. Clumps A and B are detected at an angular distance from the CSPN $\approx 75''$ along PAs $\approx 0^\circ$ and $\approx 170^\circ$, respectively, i.e., they are almost at the same distance but along opposite directions from the CSPN. Meanwhile, clump C, along PA $\approx 190^\circ$, is closer to the CSPN, at $\approx 65''$. The clumps are thus projected onto the main nebular shell, which can be encircled within an ellipse $182'' \times 168''$ in size with its major axis oriented along PA $\approx 135^\circ$ (Guerrero et al. 2003). Adopting a distance of 810 pc will locate these knots at a projected distance on the plane of the sky from the CSPN of 0.29 pc for knots A and B, and 0.26 pc for knot C. If truly contained within the main nebular shell, then clumps A and B would be within 25° of the plane of the sky, whereas clump C can reach up to 40° .

The clumps are quite noticeable in the CFHT WIRCcam H_2 and *Spitzer* IRAC images in the mid-IR 3.6 and 4.5 μm bands (see Fig. 4), much weaker in *Spitzer* IRAC images at 5.8 and 8.0 μm , and [O I], with clump A detected while clumps B and C are only marginally detected, and undetected in [O III], [S II], Bry, K_c , and in the mid-IR *Spitzer* 24 μm band. The lack of [O III] emission and detection in [O I] seem to imply material of lower ionization, yet the [N II] to $\text{H}\alpha$ ratio at their cores derived from the NOT ALFOSC images, ≈ 0.15 , is actually lower than that of the surrounding nebular material, ≈ 0.4 . The emission of the clumps is thus actually enhanced in the recombination line of $\text{H}\alpha$, but reduced in the collisionally excited lines of [O III], [N II], and [S II]. These line ratios variations can be attributed to higher electronic density and lower temperature. Furthermore, the

detection of [O I] emission in clump A and marginally in clumps B and C clearly implies the presence of neutral gas and its strong link with molecular hydrogen likewise other microstructures (e.g. NGC 7009, K 4-47, among others).

Thus the detection of the clumps in near-IR H_2 narrow-band images, but unnoticeable emission in $B\gamma$, allow to reasonably attribute the emission in the *Spitzer* IRAC bands to $H_2 \nu = 0-0$ transitions. Therefore, the clumps consist mostly of denser and colder ionized material with a significant molecular content.

We further inspected the *Spitzer* IRS spectra to search for possible H_2 emission in the mid-IR range. The left panel of Figure 5 shows the slit position of the IRS data with the source and background regions. A background-subtracted spectrum was extracted in a region covering the extension of the Owl Nebula and is shown in the right panel of Figure 5. We detect a collection of emission lines in the *Spitzer* IRS spectrum, which include [Ne III], [S III] and [O IV], but none corresponding to any of the $H_2 \nu=0-0$ series. The detection of emission lines of high excitation species is expected given the high surface temperature $T_{\text{eff}} = 93.9 \pm 5.6$ kK of its CSPN (Napiwotzki 1999).

Zoom-in images of the clumps in the relevant emission line and broad-band images, as well as in the [O III]/ $H\alpha$ ratio map, typically used to trace shocks in ionized structures and in particular in PNe (Guerrero et al. 2013), are presented in Figure 6. These images and ratio map reveal that clumps A, B, and C have different morphologies, although each is remarkably similar through the different images and ratio map, besides the varying spatial resolutions of these images. Clump A (left column in Fig. 6) consists of two compact knots aligned along a direction close but not coincident with the radial direction towards the CSPN. The innermost knot is fainter than the outermost one, which shows a diffuse and fainter broad tail-like structure extending outwards. Clump B (middle column in Fig. 6) has a compact head and a ≈ 25 arcsec long tail pointing outwards from the CSPN, with a possible broad bow-shock structure pointing inwards the nebula. Finally clump C (right column in Fig. 6) has a knotty, irregular appearance. Interestingly, the Gemini GMOS colour-composite picture of this clump reveals differences in colour, with the westernmost structures being brighter in the broad-band images, which are not apparent in the CFHT near-IR and *Spitzer* mid-IR colour-composite pictures. These westernmost structures may instead be associated with background galaxies, of which many are detected in the FoV with Gemini and *Spitzer* colours similar to these ones.

4 DISCUSSION

As mentioned in Section 1, NGC 3587 is an evolved PN and its CSPN has a high UV flux, while the nebular density is generally low, with no high density structure² capable of providing shelter for the survival of molecular material in this harsh environment. Evolved PNe with H_2 clumps usually have a large number of them (group A presented in Sect. 1), which is not the case for NGC 3587. As for the physical size of the clumps, which is $\sim 1.2 \times 10^{16}$ cm for an averaged angular radius of $1''$, it is also larger than those of knots in evolved PNe, in the range of a few 10^{15} cm.

The CFHT WIRCам and *Spitzer* IRAC IR imaging of NGC 3587 (Fig. 4) confirms the presence of molecular material in three different

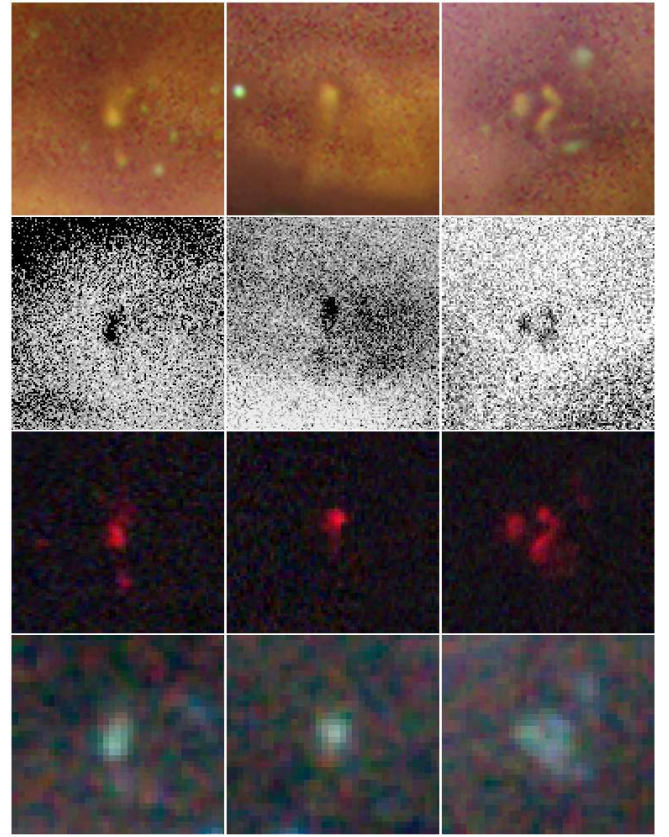


Figure 6. Colour-composite zoom-in views of the ionic low-excitation and molecular emission clumps A (left column), B (middle column), and C (right column) of NGC 3587. From top to bottom, Gemini GMOS-N $H\alpha$ + $[N II]$ (red), r -SDSS (green), and g -SDSS (blue) colour-composite picture, NOT ALFOSC $[O III]/H\alpha$ ratio maps (where black corresponds to low values of this ratio), CFHT H_2 (red), $Br\gamma$ (green) and K_c (blue) colour-composite picture, and *Spitzer* IRAC $3.6 \mu m$ (blue), $4.5 \mu m$ (green), and $8 \mu m$ (red) colour-composite picture. All frames have the same spatial scale, with a field of view of $20'' \times 20''$.

locations. Whilst no $Br\gamma$ emission is detected from ionized material in the CFHT WIRCам image, the presence of molecular hydrogen is quite obvious in Fig. 4-top and 6. Moreover, the same features are nicely detected in bluish-green colour from the nebular background in the *Spitzer* IRAC images (Fig. 4-middle and 6), suggesting that this latter features correspond to an excesses in the 3.6 and $4.5 \mu m$ bands. The emission in these bands can be attributed to the $H_2 \nu = 0-0$ forest transitions, namely S(9) to S(18), thus supporting the molecular content of these clumps.

Similar pockets of molecular material embedded within ionized material are being detected in an increasing number of PNe as the quality of their H_2 observations improves (e.g., Marquez-Lugo et al. 2013; Akas et al. 2020a). Maybe the most prominent example of these structures is the myriad of H_2 -emitting knots embedded within NGC 7293, the Helix Nebula (O'Dell, Henney, & Ferland 2007; Matsuura et al. 2007). These show morphologies that can easily match that of the knots detected in NGC 3587, as the cometary knots with tails (clump B) or multipeak knots (clump A) described by Matsuura et al. (2009). As the Owl Nebula, the Helix Nebula is an evolved PN with an estimated age of 10,000 yr (Young et al. 1999; Meaburn, López, & Richer 2008). Its hot CSPN, with a high effective temperature of $T_{\text{eff}} = 103.6 \pm 5.5$ kK (Napiwotzki 1999), confirms its evolved status. The spatial distribution of the knots in

² The structure of the Owl Nebula has been claimed to be bipolar, formed by a cylinder-like structure and a pair of cavities cleared out by one or even several fast outflows (García-Díaz et al. 2018), yet there is no evidence for a density contrast between these structures.

the Helix Nebula, along an annular or ring-like structure, is otherwise notably different to that observed in the Owl Nebula. The inner H₂-rich clumps in the Helix Nebula seem to have been sculpted during the post-AGB evolution of its progenitor star. Thus clumps and filaments would have formed as a result of hydrodynamical instabilities created during the interaction between the (fast) post-AGB and the previously ejected (slow) AGB wind.

The molecular material found in NGC 2346 provides another fair comparison with the clumps reported here in NGC 3587. High spatial resolution H₂ images reveal the true physical structure nature of its molecular material, composed of knots and filaments (Manchado et al. 2015). The formation of these structures has been proposed by means of a mechanism of depressurization in the central bubble of NGC 2346, which leads to the fragmentation of the shell into a network of knots and filaments. As the central star gets older and its UV flux declines, nebular material is not photoionized, surviving as molecular material. Instead, the spatial distribution of the H₂ clumps in the Owl Nebula is more alike that of the H₂ knots located along the periphery of the envelope of NGC 7662 (Akras, Gonçalves, & Ramos-Larios 2017).

NGC 7662 is much younger than the Owl Nebula, with a kinematic age $\approx 2,100$ yr (Guerrero, Jaxon, & Chu 2004) at the revised *Gaia* distance of 1.7 ± 0.9 kpc (Bailer-Jones et al. 2021), which may explain the larger number of H₂ clumps than those observed in the Owl Nebula, where most clumps may have already dispersed.

Clump B in NGC 3587 has the typical morphology of photoevaporated clumps seen in PNe and proplyds in the Orion Nebula (see, e.g., García-Arredondo et al. 2001): a shocked-shell surrounding the dense clump produced by the shocked photoevaporation flow, the dense clump, and the tail. Other morphologies, as those exhibited by clumps A and C, can be shaped as well as the result of the complex dynamics produced by strong ionizing sources. Indeed, the radiative-magnetohydrodynamic 3D simulations presented by Henney et al. (2009) to follow the evolution of photoevaporative flows of an initially spherical clump result in a plethora of morphologies.

The origin of molecular material in old PNe is disputed, but it is accepted that it can form by the time the AGB envelope is ejected when the star's effective temperature is low, just before the PN is born. It is difficult, however, to reconcile the short time-scale of destruction of molecules on the environment of a PN (Huggins & Maun 2002) with the evolutionary stage of NGC 3587. Hunger, Kimeswenger, & Kendl (2014) establishes two scenarios for the clumps survival: radiation and non-radiation. For the first case, they found that clumps photo-evaporate in shorter time-scales than those for the second case, where clumps are slowly destroyed by the wind. Moreover, Henney et al. (2007) set down that the main destruction processes for the H₂ molecular material is due to photoionization by extreme ultraviolet radiation, which is relevant for the case of evolved PNe with molecular material. Whatever the main mechanism might be, whether it involves winds or UV radiation, it is apparent that the clump structures would be survivors of molecular material.

Alternatively, it has been suggested that molecules and particularly H₂ can form at late times onto the surface of dust grains (Aleman & Gruenwald 2004). At any rate, the detection of clumps of material where H₂ molecules are found in evolved PNe implies that compact, high-density structures are able to survive the whole PN evolution (and even after the PN dispersal).

As for the Owl Nebula, the density of the clumps can be roughly estimated from the comparison of the H α flux of the clumps with the H α flux of the nebula, as density scales with the root square of the flux of the H I Balmer lines. Since the nebular density is ≈ 600 cm⁻³

(Cuesta & Phillips 2000) and the H α flux of the clumps is ≈ 1.5 times that of the nebula, as determined from an area of similar angular size of the clumps and the nebular H α average surface brightness, the density of the clumps is ≈ 730 cm⁻³.

The higher electron density of the clumps in NGC 3587 contrasts with the typically lower density of LIS with respect to their surrounding nebulae (e.g. Akras & Gonçalves 2016; Mari, Gonçalves & Akras 2023). At any rate, the mass of clumps A, B, and C, derived from their density and volume, would be $\approx 10^{-6}$ M_⊙, which is a tiny fraction of the ionized nebular mass.

5 CONCLUSIONS

The observations of NGC 3587 here presented reveal for the first time isolated small-scale H₂-emitting features. The emission from these elusive structures would arise from clumps of material denser than the environment around them, thus allowing molecular material either to survive the whole PN evolution or to condense onto dust grains.

Unfortunately, none of the MIR spectroscopic data available ranging between 5.2 and 38 μ m registers the small H₂ zones observed, which would have made it possible to discern the true nature of the clumps by means of the H₂ rotational emission lines, deriving the Boltzmann distribution to calculate the H₂ excitation temperature.

This evolved and well studied object can now be considered a new member of PNe with H₂ content. The persistence of this molecular material in small pockets is intriguing.

ACKNOWLEDGEMENTS

The authors thank the anonymous referee for comments and suggestions that improved the presentation of the results. GRL acknowledges support from Consejo Nacional de Ciencia y Tecnología (CONACyT) grant 263373 and Programa para el Desarrollo Profesional Docente (PRODEP) (Mexico). MAG also acknowledges support of grant PGC2018-102184-B-I00 co-funded with FEDER funds. JAT thanks support from the project UNAM PAPIIT IA101622. Based on observations obtained with WIRCcam, a joint project of CFHT, Taiwan, Korea, Canada, France, at the Canada-France-Hawaii Telescope (CFHT) which is operated by the National Research Council (NRC) of Canada, the Institut National des Sciences de l'Univers of the Centre National de la Recherche Scientifique of France, and the University of Hawaii. The Nordic Optical Telescope, operated on the island of La Palma jointly by Denmark, Finland, Iceland, Norway and Sweden, in the Spanish Observatorio del Roque de los Muchachos of the Instituto de Astrofísica de Canarias. Based on observations made with the 2.3 m Aristarchos telescope, Helmos Observatory, Greece, which is operated by the Institute for Astronomy, Astrophysics, Space Applications and Remote Sensing of the National Observatory of Athens, Greece. This research uses data obtained through the Telescope Access Program (TAP), which is funded by the National Astronomical Observatories, Chinese Academy of Sciences, and the Special Fund for Astronomy from the Ministry of Finance. This work is based in part on observations made with the Spitzer Space Telescope, which is operated by the Jet Propulsion Laboratory, California Institute of Technology under a contract with NASA. This work has made extensive use of NASA's Astrophysics Data System (ADS).

DATA AVAILABILITY

The data underlying this work will be shared on reasonable request to the corresponding author.

REFERENCES

- Akras S., Gonçalves D. R., 2016, MNRAS, 455, 930A.
- Akras S., Gonçalves D. R., Ramos-Larios G., 2017, MNRAS, 465, 1289.
- Akras S., Gonçalves D. R., Ramos-Larios G., Aleman I., 2020a, MNRAS, 493, 3800.
- Akras, S., Gonçalves, D. R., Ramos-Larios, G., et al. 2020b, *Galaxies*, 8, 30. doi:10.3390/galaxies8020030
- Aleman I., Gruenwald R., 2004, ApJ, 607, 865.
- Bailer-Jones, C. A. L., Rybizki, J., Fouesneau, M., et al. 2021, AJ, 161, 147.
- Chu, Y.-H., Gruendl, R. A., Guerrero, M. A., et al. 2009, AJ, 138, 691.
- Cuesta L., Phillips J. P., 2000, AJ, 120, 2661.
- De Marco O., Akashi M., Akras S., Alcolea J., Aleman I., Amram P., Balick B., et al., 2022, NatAs, 6, 1421.
- Fang X., Zhang Y., Kwok S., Hsia C.-H., Chau W., Ramos-Larios G., Guerrero M. A., 2018, ApJ, 859, 92.
- Fazio G. G., Hora J. L., Allen L. E., Ashby M. L. N., Barmby P., Deutsch L. K., Huang J.-S., et al., 2004, ApJS, 154, 10.
- García-Arredondo, F., Henney, W. J., & Arthur, S. J. 2001, ApJ, 561, 830.
- García-Díaz M. T., Steffen W., Henney W. J., López J. A., García-López F., González-Buitrago D., Áviles A., 2018, MNRAS, 479, 3909.
- Gledhill T. M., Froebrich D., Campbell-White J., Jones A. M., 2018, MNRAS, 479, 3759.
- Gonçalves D. R., Corradi R. L. M., Mampaso A., 2001, ApJ, 547, 302.
- Guerrero, M. A., Toalá, J. A., Medina, J. J., et al. 2013, A&A, 557, A121.
- Guerrero M. A., Chu Y.-H., Machado A., Kwitter K. B., 2003, AJ, 125, 3213.
- Guerrero M. A., Jaxon E. G., Chu Y.-H., 2004, AJ, 128, 1705.
- Guerrero M. A., Villaver E., Machado A., García-Lario P., Prada F., 2000, ApJS, 127, 125.
- Henney W. J., Williams R. J. R., Ferland G. J., Shaw G., O'Dell C. R., 2007, ApJL, 671, L137.
- Henney, W. J., Arthur, S. J., de Colle, F., et al. 2009, MNRAS, 398, 157.
- Hora J. L., Latter W. B., Deutsch L. K., 1999, ApJS, 124, 195.
- Houck J. R., Roellig T. L., van Cleve J., Forrest W. J., Herter T., Lawrence C. R., Matthews K., et al., 2004, ApJS, 154, 18.
- Huggins P. J., Maun N., 2002, A&A, 393, 273.
- Hunger L., Kimeswenger S., Kendl A., 2014, apn6.conf, 117
- Isaacman R., 1984, A&A, 130, 151
- Kastner J. H., Weintraub D. A., Gatley I., Merrill K. M., Probst R. G., 1996, ApJ, 462, 777.
- Latter W. B., Kelly D. M., Hora J. L., Deutsch L. K., 1995, ApJS, 100, 159.
- Machado A., Stanghellini L., Villaver E., García-Segura G., Shaw R. A., García-Hernández D. A., 2015, ApJ, 808, 115.
- Marquez-Lugo R. A., Ramos-Larios G., Guerrero M. A., Vázquez R., 2013, MNRAS, 429, 973.
- Marquez-Lugo R. A., Guerrero M. A., Ramos-Larios G., Miranda L. F., 2015, MNRAS, 453, 1888.
- Mari M. B., Gonçalves D. R., Akas S., 2023, MNRAS, 518, 3908M
- Mata H., Ramos-Larios G., Guerrero M. A., Nigoche-Netro A., Toalá J. A., Fang X., Rubio G., et al., 2016, MNRAS, 459, 841.
- Matsuura M., Speck A. K., Smith M. D., Zijlstra A. A., Viti S., Lowe K. T. E., Redman M., et al., 2007, MNRAS, 382, 1447.
- Matsuura M., Speck A. K., McHunu B. M., Tanaka I., Wright N. J., Smith M. D., Zijlstra A. A., et al., 2009, ApJ, 700, 1067.
- Meaburn J., López J. A., Richer M. G., 2008, MNRAS, 384, 497.
- Napiwotzki R., 1999, A&A, 350, 101.
- O'Dell C. R., Henney W. J., Ferland G. J., 2007, AJ, 133, 2343.
- Otsuka M., Ueta T., van Hoof P. A. M., Sahai R., Aleman I., Zijlstra A. A., Chu Y.-H., et al., 2017, ApJS, 231, 22.
- Puget P., Stadler E., Doyon R., Gigan P., Thibault S., Luppino G., Barrick G., et al., 2004, SPIE, 5492, 978.
- Ramos-Larios G., Guerrero M. A., Miranda L. F., 2008, AJ, 135, 1441.
- Ramos-Larios G., Guerrero M. A., Sabin L., Santamaría E., 2017, MNRAS, 470, 3707.
- Rieke G. H., Young E. T., Engelbracht C. W., Kelly D. M., Low F. J., Haller E. E., Beeman J. W., et al., 2004, ApJS, 154, 25.
- Sabbadin F., Bianchini A., Ortolani S., Strafella F., 1985, MNRAS, 217, 539.
- Smith J. D. T., Armus L., Dale D. A., Roussel H., Sheth K., Buckalew B. A., Jarrett T. H., et al., 2007, PASP, 119, 1133.
- Tody, D. 1993, *Astronomical Data Analysis Software and Systems II*, 52, 173
- Webster B. L., Payne P. W., Storey J. W. V., Dopita M. A., 1988, MNRAS, 235, 533.
- Young K., Cox P., Huggins P. J., Forveille T., Bachiller R., 1999, ApJ, 522, 387

This paper has been typeset from a \LaTeX file prepared by the author.